Liquid-metal flow in a finite-length cylinder with a high-frequency rotating magnetic field

By L. MARTIN WITKOWSKI[1], P. MARTY[2]
AND J. S. WALKER[1]

[1]Department of Mechanical and Industrial Engineering, University of Illinois,
1206 W. Green St., Urbana, IL 61801, USA

[2]Laboratoire des Ecoulements Géophysiques et Industriels, B.P. 53, 38041 Grenoble, France

A liquid-metal flow driven by a rotating magnetic field in a finite-length cylinder is studied numerically as a function of the field frequency. In the high-frequency case, the magnetic field is expelled from the liquid-metal except in a skin-depth layer along the side and top walls of the cylinder. In the corner region, where the skin-depth layers intersect, the body force exhibits a large positive and negative azimuthal component as well as inward radial and axial components which are rotational. The flows for various frequencies are compared to the low-frequency flow.

1. Introduction

Rotating magnetic fields (RMF) have been used for decades to stir molten metals during continuous casting (Moffatt 1978; Davidson 1992), and are now being used to stir molten semiconductors during growth of single crystals (Dold & Benz 1999), although this idea came up quite early as described in a pioneering work (Mullin 1958). In continuous casting, the Reynolds number is extremely large and the flow is turbulent, but applications in crystal growth involve laminar flows (Priede 1993). Most studies of flows induced by RMFs are based on two assumptions.

The first assumption is that the shielding parameter $R_\omega = \mu_p \sigma \omega R^2 \ll 1$, where μ_p and σ are the magnetic permeability and electrical conductivity of the liquid metal, ω is the circular frequency of the RMF, and R is the inside radius of the cylinder containing the liquid. With $R_\omega \ll 1$, the magnetic field produced by the electric current in the liquid is negligible compared to the magnetic field produced by the external inductor, so that the latter penetrates throughout the liquid metal (Moffatt 1965; Dahlberg 1972).

The second common assumption involves the interaction parameter $N = \sigma B^2 / \rho \omega$ and the magnetic Taylor number $Tm = \sigma \omega B^2 R^4 / 2 \rho v^2$, where B is the characteristic magnetic flux density of the RMF while ρ and v are the density and kinematic viscosity of the liquid metal. For most applications of RMFs in materials processing, N is small and Tm is large, and the second common assumption is that N is sufficiently small so that $N^{1/2} Tm^{1/6} \ll 1$. The first consequence of this latter condition is that the liquid velocity is much smaller than ωR, so that the flow has no effect on the electromagnetic variables, and there are two sequential problems (Davidson 1992). The solution of the first problem gives the electric current in the liquid, the magnetic field if R_ω is not small, and the electromagnetic (EM) body force on the liquid. The solution of the second problem gives the liquid motion produced by the EM body

force. The EM body force is the superposition of a steady axisymmetric force and a force which is periodic in both time and the azimuthal coordinate and which has a circular frequency of 2ω. The second consequence of $N^{1/2}Tm^{1/6} \ll 1$ is that the flow driven by the temporally and azimuthally periodic part of the EM body force is negligible compared to the flow driven by the steady axisymmetric part of the EM body force (Davidson & Hunt 1987; Martin Witkowski, Walker & Marty 1999).

There have been many studies of the steady axisymmetric flow in a finite-length cylinder with the assumptions that $R_\omega \ll 1$ and $N^{1/2}Tm^{1/6} \ll 1$ (for example Davidson 1991; Gelfgat, Priede & Sorkin 1991; Priede 1993; Davidson 1992). With these two assumptions, the steady part of the EM body force is in the azimuthal direction and drives a swirling azimuthal flow. A meridional flow with radial and axial velocity components is driven by the axial variation of the centrifugal force of the swirling flow and involves radially inward flows near axial boundaries where the azimuthal velocity is zero. When the viscous diffusion of momentum is much smaller than the meridional-flow momentum transport and when the azimuthal velocity is much larger than the meridional ones, the important features of the flow are determined by the total torque due to the steady EM body force, while the axial distribution of the body force is not very important (Davidson 1992).

This paper treats flows induced by high-frequency RMFs for which R_ω is not small. A typical crystal growth configuration for which this parameter is large is discussed by Spitzer (1999). Moffatt (1965) and Dahlberg (1972) treated the flow in an infinitely long cylinder with the assumption that all variables are independent of the axial coordinate and with large and arbitrary values of R_ω. When $R_\omega = O(1)$, the magnetic field produced by the axial electric current in the liquid partially cancels the magnetic field due to the external inductor in the interior of the liquid. When R_ω is large, this cancellation is complete except in a thin 'skin-depth' layer adjacent to the inside surface of the cylinder. The magnetic field, electric current and EM body force are confined to this layer which has a characteristic thickness of $RR_\omega^{-1/2}$.

Here we treat the flow in a finite-length cylinder with electrically insulated walls for arbitrary values of R_ω and with the assumption that $N^{1/2}Tm^{1/6} \ll 1$. Gelfgat, Gorbunov & Kolevzon (1993) present some experimental measurements of the velocity of a liquid mixture of indium, gallium and tin in a cylinder with a 400 Hz RMF. Unfortunately they did not give the value of B for their RMF, so quantitative comparisons with their results are not possible. Mazuruk *et al.* (1997) present an approximate solution for the RMF in a finite-length cylinder which they state is reasonably accurate for $R_\omega < 100$. They also present solutions for the liquid motion neglecting the inertial terms in the Navier–Stokes equations. Unfortunately inertial effects, specifically the meridional-flow momentum transport, are dominant rather than negligible in actual crystal-growth applications of RMFs (Priede 1993).

2. Electromagnetic body force

The ampoule containing the liquid metal has a radius R and an axial length $2hR$. The geometry with all lengths normalized by R is sketched in figure 1. We use cylindrical coordinates r, θ, z with units vectors e_r, e_θ, e_z. The z-axis is along the centreline of the cylinder. We assume that the magnetic field is produced by an infinitely long cylindrical current sheet located at a radius aR, where $a \geqslant 1$. With only small deviations from a real device, we take the magnetic permeability of the material surrounding the current sheet to be infinite. The current distribution in the sheet is idealized as $\boldsymbol{J} = -J_0 \cos{(\theta - \omega t)}\boldsymbol{e}_z$, where J_0 stands for the peak current per
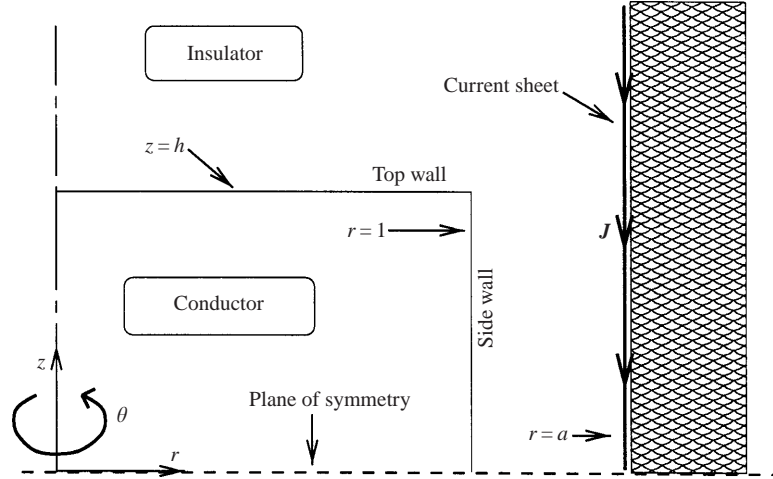
FIGURE 1. Geometry with lengths normalized by R.
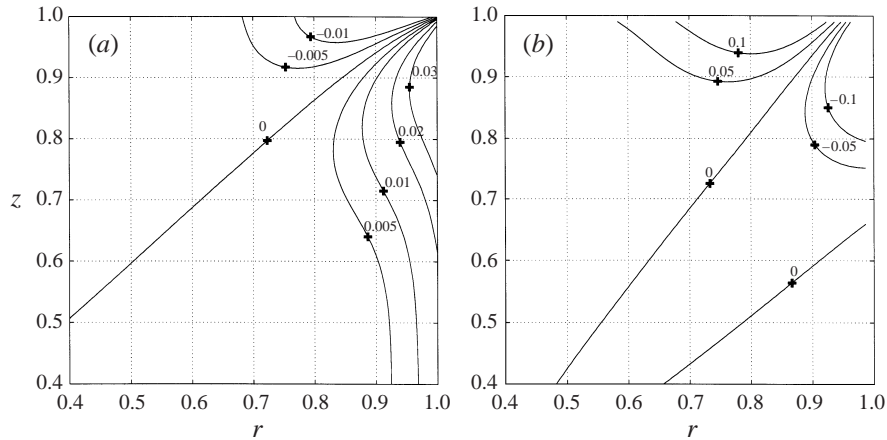
FIGURE 2. Contours plots of (a) f_θ; (b) $(\nabla \times \boldsymbol{f})_\theta$ for $h = 1$, $a = 1.6$ and $R_\omega = 150$.

unit azimuthal length and t is time. The magnetic field produced by this current sheet is uniform for $R_\omega \ll 1$.

The numerical solutions for the periodic magnetic field $\boldsymbol{B}$ and the periodic electric current density $\boldsymbol{j}$ in the liquid for any value of R_ω and for $N^{1/2}Tm^{1/6} \ll 1$ were presented in a previous paper (Martin Witkowski, Marty & Walker 2000). The electromagnetic body force $\boldsymbol{f} = \boldsymbol{j} \times \boldsymbol{B}$ involves a steady force and a periodic force with a frequency of 2ω. With our assumption that $N^{1/2}Tm^{1/6} \ll 1$, the periodic force can be neglected. The steady part of $\boldsymbol{f}$ has an azimuthal component f_θ, as well as radial and axial components f_r and f_z, the curl of which gives

$$(\nabla \times \boldsymbol{f})_\theta = \left(\frac{\partial f_r}{\partial z} - \frac{\partial f_z}{\partial r} \right) \neq 0.$$

This is a major difference from an RMF with $R_\omega \ll 1$, for which $(\nabla \times \boldsymbol{f})_\theta = 0$. Here f_θ and $(\nabla \times \boldsymbol{f})_\theta$ are normalized by $\sigma \omega R B^2/2$ and $\sigma \omega B^2/2$, respectively.

For all the results presented in this paper, $a = 1.6$ and $h = 1$. Details on the mesh

size are given in §3. For $R_\omega = 150$, the contours of f_θ and $(\nabla \times \boldsymbol{f})_\theta$ are presented in figure 2. Even for such a moderate value of R_ω, f_θ is confined to the emerging skin-depth layers with the peak values close to the corner at $r = 1, z = h$. For $R_\omega \ll 1$, $f_\theta > 0$ everywhere and the maximum is 0.74 at $r = 1, z = 0$. The negative values of f_θ near $z = h$ for $R_\omega > 1$ were previously explained by Gelfgat, Gorbunov & Kolevzon (1993), so we merely restate their explanation. For $R_\omega \ll 1$, the uniform magnetic field penetrates throughout the liquid metal, $B_z = 0$, and only positive values of f_θ are produced by j_z and B_r. For $R_\omega > 1$, the electric currents partially expel the magnetic field from the liquid metal. For the infinitely long cylinders treated by Moffatt (1965) and Dahlberg (1972), the expelled magnetic field lines must go around the cylinder in z = constant planes, so that B_z is still zero everywhere.

For a finite length cylinder, some expelled magnetic field lines still go around the periphery at $r = 1$, but some now go over the top at $z = h$. The fraction of the field lines produced by the inductor for $z \leqslant h$ which go over the top of the cylinder rather than around the periphery increases as h decreases. The deflection of the magnetic field lines over the top leads to values of B_z in the liquid metal which increase as z increases from 0 to h near $r = 1$, and then decrease as r decreases from 1 to 0 near $z = h$. For both $R_\omega \ll 1$ and $R_\omega > 1$, j_z must complete its circuit with a transverse current in the liquid metal near $z = h$. For $R_\omega \ll 1$, this transverse current does not produce an azimuthal body force because $B_z = 0$, but for $R_\omega > 1$, this transverse current interacts with the B_z from the magnetic field lines going over the top of the cylinder to produce $f_\theta < 0$ near $z = h$.

Figure 3 presents projections of the magnetic field and electric current density vectors in the $(\theta - \omega t = -\pi/2)$-plane for $R_\omega = 150$ and for two points at $r = 1$ and for two points at $z = h = 1$. The transverse current $j_r > 0$ at $z = 1$ turns to flow axially downward with $j_z < 0$ at $r = 1$. As z increases at $r = 1$, the number of magnetic field lines deflected over the top accumulates so that the magnitudes of B_r and B_z increase. As r decreases from 1 at $z = 1$, the field lines which have cut across the corner of the liquid metal at $r = z = 1$ become parallel to the top. Clearly $\boldsymbol{j} \times \boldsymbol{B}$ produces $f_\theta > 0$ near $r = 1$ and the positive value of f_θ increases with increasing z until very close to $z = 1$ where $j_z = 0$. Similarly $\boldsymbol{j} \times \boldsymbol{B}$ produces a negative value of f_θ near $z = 1$, but the magnitude of f_θ quickly decreases as r decreases and $\boldsymbol{B}$ becomes parallel to $\boldsymbol{j}$.

For $R_\omega \gg 1$, the liquid metal can be divided into a core region where $\boldsymbol{B} = \boldsymbol{j} = 0$ to all orders in R_ω, a skin-depth layer with $O(R_\omega^{-1/2})$ thickness adjacent to the side at $r = 1$ where $B_r = O(R_\omega^{-1/2})$ while B_θ and $B_z = O(1)$, a skin-depth layer with $O(R_\omega^{-1/2})$ thickness adjacent to the top at $z = h = 1$ where B_r and $B_\theta = O(1)$ while $B_z = O(R_\omega^{-1/2})$, and a corner region with $\Delta r = O(R_\omega^{-1/2})$ and $\Delta z = O(R_\omega^{-1/2})$ at $r = 1$, $z = h$. If $R_\omega = \infty$, B_r and B_z in the electrical insulators become infinite at $r = 1, z = h$, namely they behave like $\xi^{-1/3}$ where $\xi = [(r-1)^2 + (z-h)^2]^{1/2}$. This follows from the solution of the Laplace equation for an external right-angle corner, e.g. ideal-fluid flow over such a corner without separation (White 1999). In fact B_r and B_z do not become infinite because the magnetic field lines can cut across the corner region in the liquid metal. Thus we conclude that B_r and B_z become $O((R_\omega^{-1/2})^{-1/3}) = O(R_\omega^{1/6})$ in the corner region and in the adjacent $O(R_\omega^{-1/2}) \times O(R_\omega^{-1/2})$ part of the electrical insulator.

For $R_\omega \ll 1$, B_r is independent of r and z, and $B_z = 0$, so that the maximum f_θ corresponds to the maximum $|j_z|$ at $r = 1, z = 0$. For $R_\omega > 1$, $f_\theta = j_z B_r - j_r B_z$ depends on the variations of both $\boldsymbol{j}$ and $\boldsymbol{B}$. As z increases near $r = 1$, the increase in $-B_r$ from $O(R_\omega^{-1/2})$ to $O(R_\omega^{1/6})$ is much larger than the decrease of $-j_z$, so f_θ increases
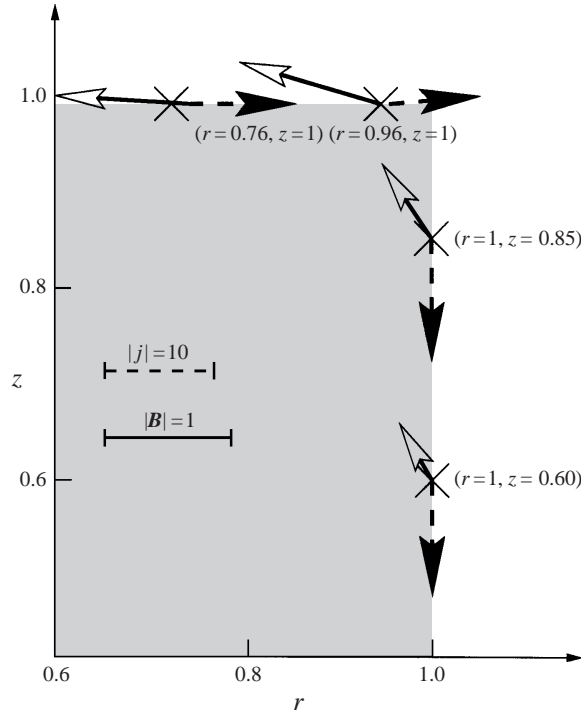
FIGURE 3. Projections in the $(\theta - \omega t = -\pi/2)$-plane of some magnetic field (solid line and open arrow) and current density (dash dotted and solid arrow) vectors in the corner region for $R_\omega = 150$.

until very close to $z = h$ where $j_z = 0$ and $f_\theta = 0$. Similarly as r increases near $z = h$, the increase in B_z from $O(R_\omega^{-1/2})$ to $O(R_\omega^{1/6})$ is much greater than the decrease in j_r, so that $-f_\theta$ increases, until very close to $r = 1$, where $j_r = f_\theta = 0$. Since $j_r = O(R_\omega^{-1/2})$ in the skin-depth layer at $z = h$ and in the corner region, while $j_z = O(R_\omega^{-1/2})$ in the skin-depth layer at $r = 1$ and in the corner regions, the magnitudes of both the positive and negative values of f_θ scale as R_ω^{-1} for the two skin-depth layers and $R_\omega^{-1/3}$ for the corner region. We present the evolution of the maximum and minimum value of f_θ as well as the value of f_θ on the side and top layer as a function of R_ω in figure 4.

The second change from $R_\omega \ll 1$ is that $(\nabla \times \boldsymbol{f})_\theta$ is no longer zero. For the low-frequency case, the average over one period of the radial or axial body force is zero because there is a phase shift of one quarter-period between the components of $\boldsymbol{j}$ and $\boldsymbol{B}$ which produce f_r and f_z. We present in figure 5 plots of $-f_r$ and $-f_z$ in the skin-depth layer. As the frequency is increased, the phase shift decreases from one-quarter to one-eighth of a period but this change in phase shift only occurs for the inward force near each surface. For $R_\omega \gg 1$ near $r = 1$, the phase shift for f_z is a quarter-period, so that the local steady f_z is zero, while the phase shift for f_r has changed to an eighth-period, giving a radially inward body force near $r = 1$. Similarly for $R_\omega \gg 1$ near $z = h$, the phase shift for f_r is still a quarter-period, while that for f_z has changed to an eighth-period. In the corner region, both f_r and f_z involve a change in phase shift and give a large force toward the centre of the liquid metal. For an infinite cylinder with $R_\omega > 1$, there is an inward force $f_r < 0$ but it is independent of z so $(\nabla \times \boldsymbol{f})_\theta = 0$. For a finite length cylinder, $-f_r$ near $r = 1$ increases as z increases from 0 to h and $-f_z$ near $z = h$ increases as r increases from 0 to 1, so that
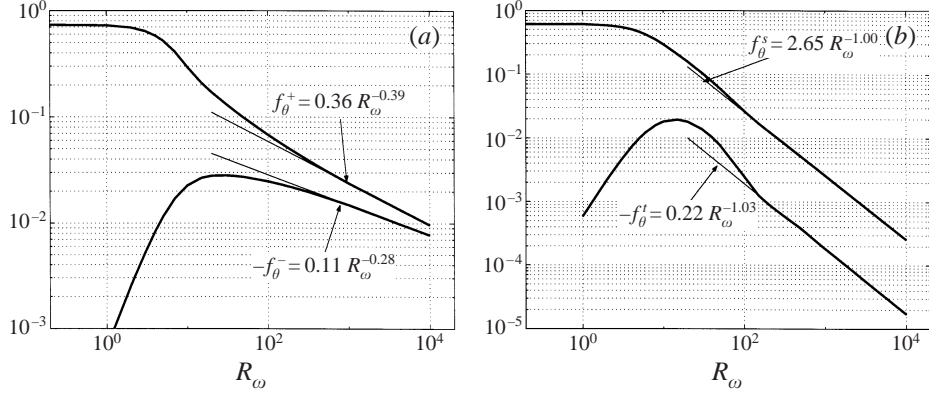
FIGURE 4. Azimuthal body force as a function of R_ω: (a) maximum value f_θ^+ and minimum value f_θ^-, (b) $f_\theta^t = f_\theta$ $(r = 0.5, z = 1)$ and $f_\theta^s = f_\theta$ $(r = 1, z = 0.5)$.
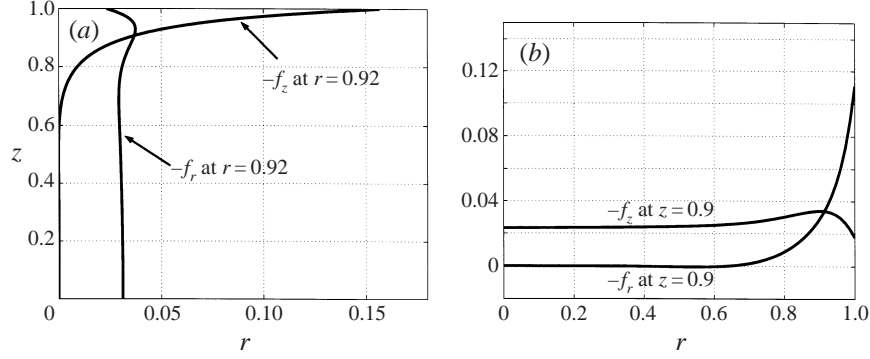
FIGURE 5. Plots of (a) $-f_r$ and $-f_z$ close to the sidewall; (b) $-f_r$ and $-f_z$ close to the top wall for $h = 1$, $a = 1.6$ and $R_\omega = 150$.

$(\nabla \times \boldsymbol{f})_\theta$ drives two toroidal cells of meridional flow for $z > 0$, both with flow along $r = 1$ or along $z = h$ toward the corner, flow from the corner toward the centre of the liquid metal and finally flow in the interior back toward $r = 1$ or $z = h$ to complete both circulations.

We represent in figure 6 the evolution of the integral

$$I = 4\pi \int_0^h \int_0^1 |(\nabla \times \boldsymbol{f})_\theta| \, r \, \mathrm{d}r \, \mathrm{d}z \qquad (2.1)$$

as a function of R_ω, which reveals the magnitude of the rotational body force. It has a maximum value at approximately $R_\omega = 6.5$. For this value of R_ω all three components of the body force have approximately the same magnitude. As R_ω becomes larger, the magnitudes of f_r and f_z become $O(R_\omega^{-1/6})$ in the corner region and are therefore larger than the $O(R_\omega^{-1/3})$ f_θ in the corner region. For $R_\omega \gg 1$, the largest contribution to the integral I in (2.1) comes from the corner region and is $O(R_\omega^{-2/3})$, but the value of the integral has not yet approached this behaviour when $R_\omega = 1000$. Mazuruk *et al.* (1997) did compare the magnitude of the driving force for the meridional flow to that of the driving force for the azimuthal flow. This comparison is appropriate for the viscous regime but for the inertial flow regime, which is our primary interest here,
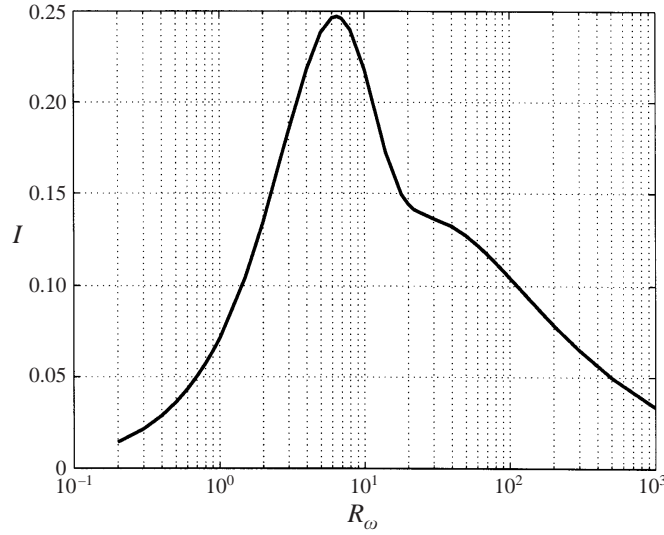
FIGURE 6. Integral I as a function of R_ω.

the relative importance of driving forces for the meridional flow is given, as shown in (3.2*b*), by the ratio of $(\partial/\partial z)(\Gamma^2/r^3)$ to $(\nabla \times \boldsymbol{f})_\theta$. This important ratio of source terms for the meridional flow can only be analysed after the flow is known, and is discussed in the next section.

3. Flow problem

3.1. *Problem formulation*

With $N^{1/2} Tm^{1/6} \ll 1$, the Navier–Stokes equations reduce to equations governing the meridional flow stream function ψ, the azimuthal vorticity Ω and the angular momentum Γ, which are related to the dimensionless velocity $\boldsymbol{V} = v_r \boldsymbol{e}_r + v_\theta \boldsymbol{e}_\theta + v_z \boldsymbol{e}_z$ by

$$v_r = \frac{1}{r} \frac{\partial \psi}{\partial z}, \quad v_z = -\frac{1}{r} \frac{\partial \psi}{\partial r}, \quad \Gamma = r v_\theta, \quad \Omega = \frac{\partial v_r}{\partial z} - \frac{\partial v_z}{\partial r}. \tag{3.1a–d}$$

The Navier–Stokes equations reduce to

$$\frac{\partial^2 \psi}{\partial r^2} - \frac{1}{r} \frac{\partial \psi}{\partial r} + \frac{\partial^2 \psi}{\partial z^2} = r\Omega, \tag{3.2a}$$

$$\frac{\partial \Omega}{\partial t} + \frac{\partial (v_r \Omega)}{\partial r} + \frac{\partial (v_z \Omega)}{\partial z} - \frac{\partial}{\partial z} \left(\frac{\Gamma^2}{r^3} \right) = \Delta\Omega + Tm \, (\nabla \times \boldsymbol{f})_\theta, \tag{3.2b}$$

$$\frac{\partial \Gamma}{\partial t} + \frac{\partial (v_r \Gamma)}{\partial r} + \frac{v_r \Gamma}{r} + \frac{\partial (v_z \Gamma)}{\partial z} = \left(\frac{\partial^2 \Gamma}{\partial r^2} - \frac{1}{r} \frac{\partial \Gamma}{\partial r} + \frac{\partial^2 \Gamma}{\partial z^2} \right) + Tm \, r f_\theta, \tag{3.2c}$$

where V, ψ, Γ and Ω are normalized with a viscous velocity scale ν/R and R. Since the flow is symmetric about the plane at $z = 0$, we treat only $z > 0$ with the boundary conditions

$$\Gamma(0, z) = \Gamma(r, h) = \Gamma(1, z) = 0, \tag{3.3a}$$

$$\psi(0, z) = \psi(r, h) = \psi(1, z) = 0, \tag{3.3b}$$

$$\frac{\partial \psi}{\partial r}(1, z) = \frac{\partial \psi}{\partial z}(r, h) = 0, \tag{3.3c}$$

where $r \in [0, 1]$ and $z \in [0, h]$. The stream function ψ (and as consequence the vorticity Ω) is an odd function of z while the angular momentum Γ is even. The evaluation of the vorticity on the wall results from equation (3.2a) along with (3.3b) and (3.3c) giving

$$\Omega(0, z) = 0, \quad \Omega(1, z) = \frac{\partial^2 \psi}{\partial r^2}(1, z), \quad \Omega(r, h) = \frac{1}{r}\frac{\partial^2 \psi}{\partial z^2}(r, h). \tag{3.4}$$

This time-dependent set of equations for the fluid flow problem has been solved with a classical ADI (alternating direction implicit) scheme in time and a second-order finite difference scheme in space. The vorticity on the boundary is computed using the Thom formula. As an example for the top wall: $r_i\Omega_{i,w} = 2\psi_{i,w-1}/(\Delta z)^2$ where subscript i is the index for the radial grid, w is the index for the wall and Δz the axial mesh size. This first-order approximation to (3.4) is in fact a second-order-accurate approximation to (3.3c). This topic is discussed by Spotz (1998). The technique used is derived from the work of Sørensen & Phuoc Loc (1989). The main changes were to add the electromagnetic body force and to simplify the code using a regular grid and a second-order accurate solver from FISHPACK (Sweet 1977) for the Poisson equation (3.2a) instead of the solver based on a fourth-order Hermitian approximation used in the original work.

We had to ensure that both the skin-depth layer and the Bödewadt-like layer were properly resolved. For simplicity and to avoid spurious results due to interpolation, we used the same mesh for the electromagnetic and the flow computations. In the low-frequency case (i.e $R_\omega \ll 1$), the Bödewadt-like layer on the top wall is the most restrictive condition while for the large-frequency case the skin-depth layers on both the side and top walls require a fine grid. We choose the mesh size so that at least 5 or 6 points are included in each layer. In §3.2, we present calculations for $R_\omega = 0, 20, 100, 150, 300, 1000$. The corresponding meshes chosen are ($nr \times nz = 76 \times 101$) for the first four values of R_ω, ($nr \times nz = 106 \times 141$) for $R_\omega = 300$ and ($nr \times nz = 166 \times 221$) for the last. The variables nr and nz are respectively the number of grid points in the radial and axial direction including the boundary points. In order to keep the flow in an inertial regime, we adjust the value of Tm so that the maximum value of v_θ is 500. While we are only interested in a steady-state solution, we integrate our double-precision computation to the regime where no variations (to machine precision) were observed between two successive time steps in the time-stepping code. The only exception to that is the result for $R_\omega = 20$ where no stable steady state could be reached. We then used a different iterative code based on the Newton method that computes only steady solutions to obtain the result presented for this particular value of R_ω. The study of the stability or multiplicity of solutions is beyond the scope of the present paper. The stability analysis is currently limited to the low-frequency case and axisymmetric disturbances for the confined geometry (Grants & Gerbeth 2001) or to radially unbounded domains for non-axisymmetric disturbances (Lingwood 1997).

3.2. *Results for the velocity field*

The evolution of the flow for increasing R_ω is presented in figures 7 and 8. In figure 7, as R_ω is increased, the location of the maximum value of v_θ moves from $r = 0.83$ and $z = 0$ for $R_\omega = 0$ to $r = 0.97$ and $z = 0.93$ for $R_\omega = 1000$. This location has already moved to $z = 0.65$ by $R_\omega = 20$. The maximum value of v_θ is following the maximum value of f_θ, as illustrated by figure 2(a). For $R_\omega = 0$, v_θ is close to a linear variation with r for $0 < r < 0.7$ and $0 < z < 0.7$. As R_ω is increased, v_θ for $r < 0.5$ decreases,
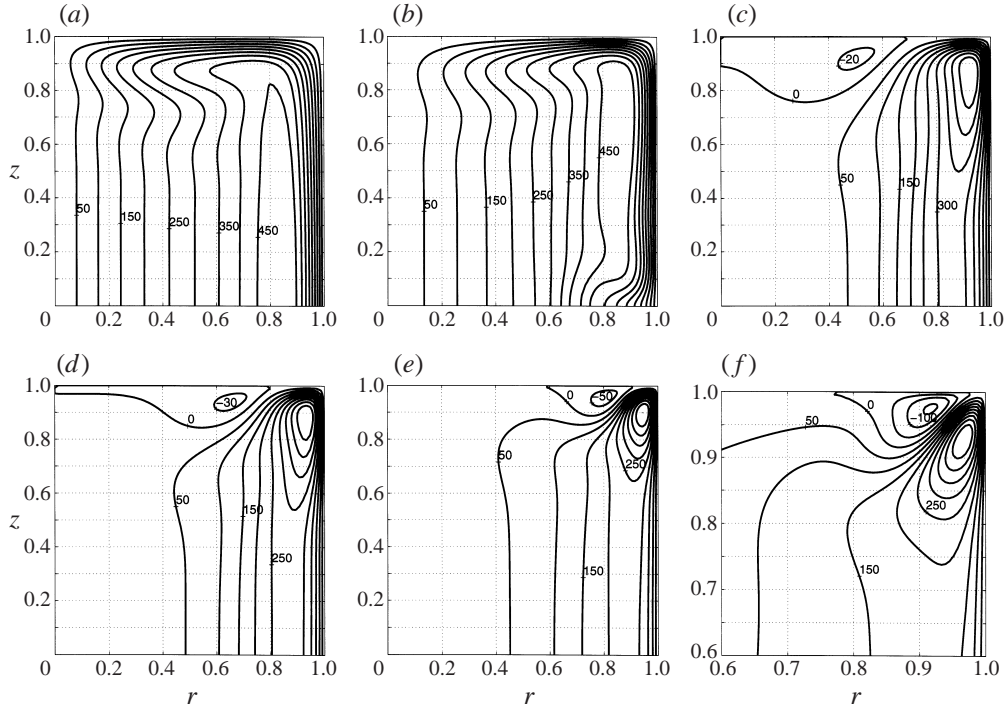
FIGURE 7. Evolution of the contours of v_θ with R_ω. (a) $R_\omega = 0$, $Tm = 5.57 \times 10^4$, $v_\theta = 50k$ for $k = 1$ to 9; (b) $R_\omega = 20$, $Tm = 4.17 \times 10^5$, $v_\theta = 50k$ for $k = 1$ to 9; (c) $R_\omega = 100$, $Tm = 4.32 \times 10^6$, $v_\theta = -20$ and $50k$ for $k = 0$ to 9; (d) $R_\omega = 150$, $Tm = 7.62 \times 10^6$, $v_\theta = -30$ and $50k$ for $k = 0$ to 9; (e) $R_\omega = 300$, $Tm = 2.06 \times 10^7$, $v_\theta = 50k$ for $k = -1$ to 9; (f) $R_\omega = 1000$, $Tm = 1.34 \times 10^8$, $v_\theta = 50k$ for $k = -3$ to 9.

and there is no azimuthal motion at these small radii for large values of R_ω. While the maximum value of v_θ is located near $r = 1$ and $z = h$ for $R_\omega \geqslant 100$, there are still significant values of v_θ for $0.5 < r < 1$ and $z < 0.6$, and these values are nearly independent of z. The values of f_θ in this region are also nearly independent of z, as indicated in figure 2(a).

In figure 7(c), there are small negative values of v_θ near $z = h$ for $r < 0.7$. This reverse azimuthal motion is clearly associated with the negative values of f_θ in figure 2(a), but the minimum value of v_θ occurs at a smaller radius than the minimum value of f_θ for $R_\omega = 100$. Near $r = 1$ and $z = h$, the meridional convection of positive angular momentum from the region with $f_\theta > 0$ dominates over the negative f_θ for $R_\omega = 100$. As R_ω is increased from 100, the minimum value of v_θ becomes larger and moves radially outward, reflecting an increasing dominance of $f_\theta < 0$ over the meridional convection of positive v_θ. For $R_\omega = 1000$, the minimum value of v_θ is located at $r = 0.92$ and $z = 0.98$, and its magnitude is nearly a third of the maximum value of v_θ. This reflects the fact that very large positive and negative values of f_θ occur in the $R_\omega^{-1/2} \times R_\omega^{-1/2}$ corner region for $R_\omega \gg 1$. Gelfgat et al. (1993) found reverse azimuthal motion near $z = h$ in their experiments with a 400 Hz RMF. In the inertialess numerical results of Mazuruk et al. (1997), $v_\theta < 0$ near $z = h$ for $R_\omega > 1$. Their analysis would predict a region with $v_\theta < 0$ for $R_\omega = 20$, but figure 7(b) shows that the radially inward convection of positive angular momentum near $z = h$ completely overwhelms $f_\theta < 0$ for $R_\omega = 20$ in the inertial regime.
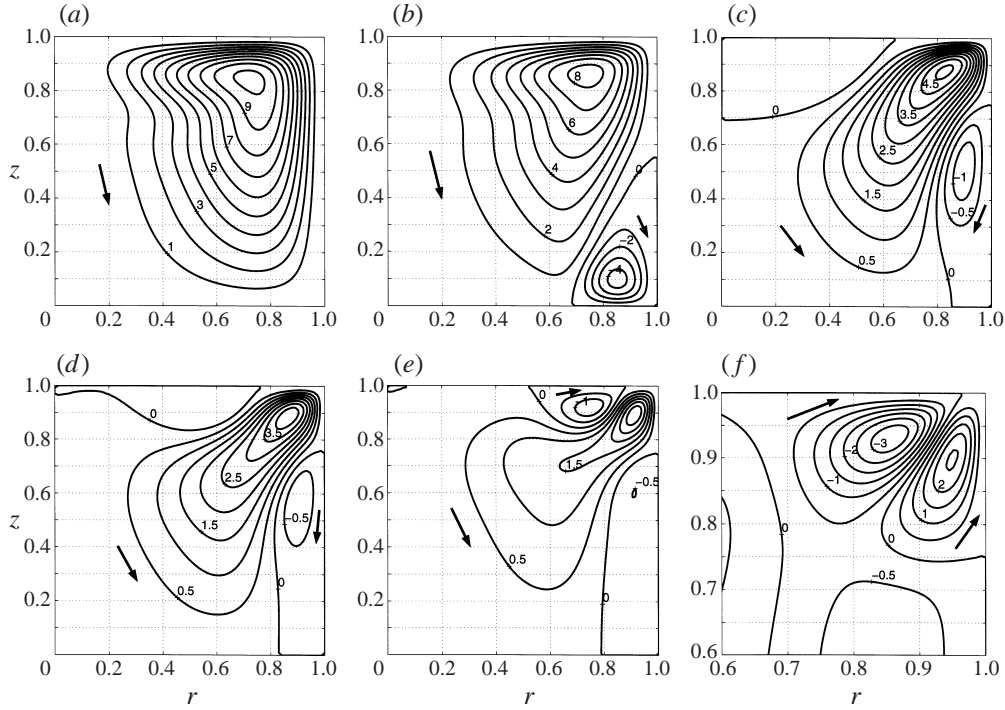
FIGURE 8. Evolution of the contours of ψ with R_ω. (a) $R_\omega = 0$, $Tm = 5.57 \times 10^4$, $\psi = k$ for $k = 1$ to 10; (b) $R_\omega = 20$, $Tm = 4.17 \times 10^5$, $\psi = k$ for $k = -4$ to 8; (c) $R_\omega = 100$, $Tm = 4.32 \times 10^6$, $\psi = 0.5k$ for $k = -2$ to 10; (d) $R_\omega = 150$, $Tm = 7.62 \times 10^6$, $\psi = 0.5k$ for $k = -1$ to 8; (e) $R_\omega = 300$, $Tm = 2.06 \times 10^7$, $\psi = 0.5k$ for $k = -2$ to 6; (f) $R_\omega = 1000$, $Tm = 1.34 \times 10^8$, $\psi = 0.5k$ for $k = -6$ to 5.

Positive and negative values of ψ represent respectively counterclockwise and clockwise circulations in the (r, z)-plane. In figure 8(a) for $R_\omega = 0$, there is a single counterclockwise meridional circulation with radially inward flow near $z = h$. Since $(\nabla \times \boldsymbol{f})_\theta = 0$ for $R_\omega = 0$, this meridional circulation is driven by the negative values of $\partial(v_\theta^2)/\partial z$ near $z = h$. As the radially inward flow inside the Bödewadt-like boundary layer at $z = h$ turns to flow axially downward, there are spatial oscillations in both the meridional streamlines in figure 8(a) and the values of v_θ in figure 7(a). These spatial oscillations are typical of flows leaving boundary layers with large angular momentum, e.g. Bödewadt and Ekman layers. The meridional flow for $R_\omega \ll 1$ has been described by Davidson (1992).

As R_ω is increased from zero, the meridional flow is affected both by the emergence of non-zero values of $(\nabla \times \boldsymbol{f})_\theta$, whose magnitude is illustrated in figure 6, and by the evolution of the spatial distribution of $\partial(v_\theta^2)/\partial z$, as illustrated in figure 7. As R_ω is increased in figure 8, the counterclockwise meridional circulation moves upward and outward toward the corner at $r = 1$ and $z = h$. For $R_\omega = 20$ in figure 8(b), there is less meridional flow for $r < 0.3$ because the values of v_θ here have decreased, and there is less inward driving force near $z = h$ for $r < 0.3$. The maximum value of v_θ has moved upward to $z = 0.65$ in figure 7(b), so that $\partial(v_\theta^2)/\partial z > 0$ for $z < 0.65$ and $r > 0.8$. This drives a clockwise meridional circulation for $r > 0.7$ and $z < 0.5$ in figure 8(b). The radially inward flow near $z = 0$ in figure 8(b) convects low-angular-momentum fluid away from the wall at $r = 1$, leading to the inward deflection of the v_θ contours
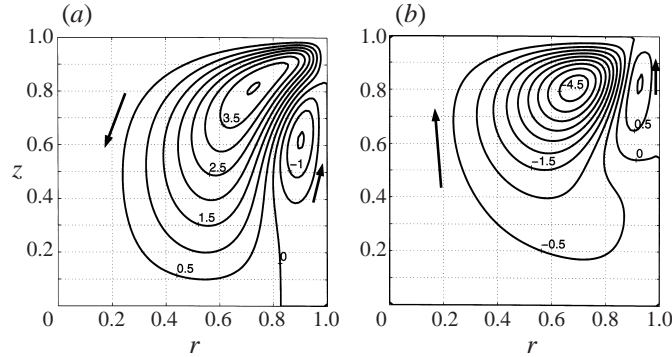
FIGURE 9. Contours of ψ for $R_\omega = 150$ and $Tm = 7.62 \times 10^6$ with (a) $(\nabla \times \mathbf{f})_\theta = 0$, (b) $f_\theta = v_\theta = 0$. (a) $\psi = 0.5k$ for $k = -3$ to 8, (b) $\psi = 0.5k$ for $k = -9$ to 2.

near $z = 0$ for $r > 0.6$ in figure 7(b). Time-dependent flow probably emerges from the instability of this clockwise circulation near $r = 1$ and $z = 0$.

For $R_\omega = 100$ in figure 8(c), the counterclockwise meridional circulation has moved toward $r = 1$ and $z = h$ and is confined between two clockwise circulations. The clockwise circulation near $r = 1$ has moved upward as the maximum value of v_θ has moved upward, so that now $\partial(v_\theta^2)/\partial z > 0$ for $z < 0.87$ and $r > 0.8$. The clockwise circulation near $z = h$ is being driven both by the $(\nabla \times \mathbf{f})_\theta > 0$ in figure 2(b) and by the region where $\partial(v_\theta^2)/\partial z > 0$ above the $v_\theta = 0$ contour in figure 7(c). As R_ω is increased from 100 in figures 8(d) and 8(e), the counterclockwise meridional circulation continues to diminish in magnitude and to move toward the corner, the clockwise circulation near $r = 1$ becomes weaker, and the clockwise circulation near $z = h$ becomes stronger and moves radially outward. For $R_\omega = 1000$ in figure 8(f), the meridional velocity inside the $R_\omega^{-1/2} \times R_\omega^{-1/2}$ corner region near $r = 1$ and $z = h$ is much larger than the meridional velocity elsewhere. The counterclockwise circulation has moved into the lower right part of the corner region, while the clockwise circulation has moved into the upper left part and has become stronger than the counterclockwise circulation.

The ratio of the integral I, defined by equation (2.1), to

$$\frac{4\pi}{Tm} \int_0^h \int_0^1 \left| \frac{\partial v_\theta^2}{\partial z} \right| \, \mathrm{d}r \, \mathrm{d}z \qquad (3.5)$$

is a characteristic ratio of the source terms, $(\nabla \times \mathbf{f})_\theta$ and $\partial(\Gamma^2/r^3)/\partial z$, in the azimuthal vorticity transport equation (3.2b). This ratio increases monotonically as R_ω is increased and has the values 0, 0.03, 0.58, 0.97, 2.1 and 8.6 for $R_\omega = 0, 20, 100, 150, 300$ and 1000, respectively. For $R_\omega \leqslant 20$, the axial variation of azimuthal velocity is the dominant source term, and for $R_\omega = 1000$, $(\nabla \times \mathbf{f})_\theta$ is the dominant source term. Indeed, the two meridional circulations in figure 8(f) coincide with the positive and negative values of $(\nabla \times \mathbf{f})_\theta$ for $R_\omega = 1000$.

We can explore the dependence of the meridional flow on these two source terms by artificially setting each term equal to zero. We illustrate this for $R_\omega = 150$ when our characteristic ratio indicates that the roles of the two source terms are equal. The meridional streamlines with $(\nabla \times \mathbf{f})_\theta = 0$ and with the f_θ term present for $R_\omega = 150$ are shown in figure 9(a). The only significant difference between figures 8(d) and 9(a) is the absence of the clockwise circulation near $z = h$ in figure 9(a), indicating

that this circulation is produced by $(\nabla \times \boldsymbol{f})_\theta$. The magnitudes of the counterclockwise circulation and of the clockwise circulation near $r = 1$ are nearly the same, indicating that both of these circulations are driven by the axial variation of azimuthal velocity, with only small effects due to $(\nabla \times \boldsymbol{f})_\theta$, even though the characteristic ratio of the two source terms is 1. Davidson *et al.* (1999) came to a similar conclusion.

The meridional streamlines with $f_\theta = 0$ and with the $(\nabla \times \boldsymbol{f})_\theta$ term present for $R_\omega = 150$ are shown in figure 9(*b*), while $v_\theta = 0$. The two circulations in figure 9(*b*) are roughly equal to those in figure 9(*a*), but the directions are opposite. The only similarity between the streamlines in figures 8(*d*) and 9(*b*) is the small clockwise circulation near $z = h$ in figure 8(*d*). We conclude that the meridional circulation for $R_\omega = 150$ is dominated by the axial variation of azimuthal velocity in spite of the fact that the characteristic ratio is 1. The source term $(\nabla \times \boldsymbol{f})_\theta$ does not become dominant until $R_\omega = 1000$. There are some similarities between figures 8(*f*) and 9(*b*), namely a strong clockwise circulation above and to the left of a weaker counterclockwise circulation, both being close to the corner at $r = 1$ and $z = h$.

4. Conclusions

This paper is focused on the evolution of the flow driven by an RMF as R_ω is increased for a fixed Reynolds number. The changes occur because there is a spatial redistribution of the azimuthal body force toward the corner at $r = 1$ and $z = h$ and because the radial and axial body forces involve a non-zero curl which drives flows along both $r = 1$ and $z = h$ toward the corner. Davidson, Short & Kinnear (1995) state (i) that the lack of importance of the axial distribution of f_θ depends on the coupling between an inviscid central core and a Bödewadt-like layer, and (ii) that this argument fails when the boundary becomes parallel to the axis of rotation so that there is no Bödewadt-like layer. The results here indicate that the axial distribution of f_θ is important near $r = 1$. For $R_\omega \geqslant 100$, the significant values of both f_θ and $(\nabla \times \boldsymbol{f})_\theta$ are confined to the corner region near $r = 1$ and $z = h$, and most of the flow becomes concentrated in this corner region as R_ω is increased to 1000. The scale for the meridional velocities is difficult to evaluate since both $(\nabla \times \boldsymbol{f})_\theta$ and $\partial(\Gamma^2/r^3)/\partial z$ compete to drive the flow so that it fails to exhibit a clear regime dependence. Nevertheless, the numerical results show that the flow rate of the meridional motion has diminished but the maximum velocities are still comparable to those in figures 8(*a*) and 8(*f*) .

The motivation for this research was to determine if a high-frequency RMF would be better than a low-frequency RMF for crystal-growth processes. Our results generally indicate that a high-frequency RMF would produce a less desirable flow in the molten semiconductor. One objective of an RMF is to provide good mixing over the entire melt. The meridional circulation in figure 8(*a*) for $R_\omega = 0$ provides the most extensive mixing, while the mixing becomes progressively more concentrated near the corner as R_ω is increased. Periodic flows are undesirable in crystal growth because they produce spatial oscillations in the concentration of the additive or dopant in the crystal. Since with a fixed Reynolds number, the flow become periodic when R_ω is increased from 0 to 20, low-frequency RMFs again appear to be better.

REFERENCES

DAHLBERG, E. 1972 On the action of a rotating magnetic field on a conducting liquid. *Tech. Rep.* AE–447. Aktiebolaget Atomenergi, Studsvik, Sweden.

DAVIDSON, P. A. 1991 Electromagnetic stirring of steel and aluminium. In *Magnetohydrodynamics in Process Metallurgy* (ed. J. Szekely, J. W. Evans, K. Blazek & N. El-Kaddah), pp. 241–249. The Minerals, Metals and Materials Society.

DAVIDSON, P. A. 1992 Swirling flow in an axisymmetric cavity of arbitrary profile, driven by a rotating magnetic field. *J. Fluid Mech.* **245**, 669–699.

DAVIDSON, P. A. & HUNT, J. C. R. 1987 Swirling recirculating flow in a liquid-metal column generated by a rotating magnetic field. *J. Fluid Mech.* **185**, 67–106.

DAVIDSON, P. A., KINNEAR, D., LINGWOOD, R. J., SHORT, D. J. & HE, X. 1999 The role of Ekman pumping and the dominance of swirl in confined flows driven by Lorentz forces. *Eur. J. Mech.* B/*Fluids* **18**, 693–711.

DAVIDSON, P. A., SHORT, D. J. & KINNEAR, D. 1995 The role of Ekman pumping in confined, electromagnetically-driven flows. *Eur. J. Mech.* B/*Fluids* **14**, 795–821.

DOLD, P. & BENZ, K. 1999 Rotating magnetic fields: fluid flow and crystal growth applications. *Prog. Cryst. Growth Charact. Mat.* **38** (1–4), 7–38.

GELFGAT, Y. M., GORBUNOV, L. A. & KOLEVZON, V. 1993 Liquid metal flow in a finite-length cylinder with a rotating magnetic field. *Exps. Fluids* **15**, 411–416.

GELFGAT, Y. M., PRIEDE, J. & SORKIN, M. 1991 Numerical simulation of MHD flow induced by magnetic field in cylindrical container of finite length. In *Proc. 1st. Intl Conf. Energy Transfer in Magnetohydrodynamic Flows, Cadarache* (ed. A. Alemany, G. Marbach & Ph. Marty), pp. 181–186. Plenum.

GRANTS, I. & GERBETH, G. 2001 Stability of axially symmetric flow driven by a rotating magnetic field in a cylindrical cavity. *J. Fluid Mech.* **431**, 407–425.

LINGWOOD, R. J. 1997 Absolute instability of the Ekman layer and related rotating flows. *J. Fluid Mech.* **331**, 405–428.

MARTIN WITKOWSKI, L., MARTY, P. & WALKER, J. S. 2000 Multidomain analytical-numerical solution for a rotating magnetic field with a finite-length conducting cylinder. *IEEE Trans. Magn.* **36**, 452–460.

MARTIN WITKOWSKI, L., WALKER, J. S. & MARTY, P. 1999 Nonaxisymmetric flow in a finite-length cylinder with a rotating magnetic field. *Phys. Fluids* **11**, 1821–1826.

MAZURUK, K., RAMACHANDRAN, N., VOLZ, M. P. & GILLIES, D. 1997 Study of frequency effects of a rotating magnetic field on fluid flow in vertical cylinders. In *Materials Research in Low Gravity* (ed. N. Ramachandran), vol. 3123, pp. 262–270. Soc. of Photo-optical Instrum. Engng, San Diego.

MOFFATT, H. K. 1965 On fluid flow induced by a rotating magnetic field. *J. Fluid Mech.* **22**, 521–528, and corrigendum **58** (1973), 823.

MOFFATT, H. K. 1978 Rotation of a liquid metal under the action of a rotating magnetic field. In *Proc. Second Bat–Sheva International Seminar, Beersheva* (ed. H. Branover & A. Yakhot), pp. 45–62. Israel Universities Press.

MULLIN, J. B. 1958 On the use of electromagnetic stirring in zone refining. *J. Electron. Control* **2** (4), 170–174.

PRIEDE, J. 1993 Theoretical study of a flow in an axisymmetric cavity of finite length, driven by a rotating magnetic field. PhD thesis, Institute of Physics, Latvian Academy of Science, Salaspils.

SØRENSEN, J. N. & PHUOC LOC, T. 1989 High-order axisymmetric Navier–Stokes code: Description and evaluation of boundary conditions. *Intl J. Numer. Meth. Fluids* **9**, 1517–1537.

SPITZER, K. H. 1999 Application of rotating magnetic fields in Czochralski crystal growth. *Prog. Cryst. Growth Charact. Mat.* **38** (1–4), 39–58.

SPOTZ, W. F. 1998 Accuracy and performance of numerical wall boundary conditions for steady, 2d, incompressible streamfunction vorticity. *Intl J. Numer. Meth. Fluids* **28**, 737–757.

SWEET, R. 1977 A cyclic reduction algorithm for solving block tridiagonal systems of arbitrary dimensions. *SIAM J. Numer. Anal.* **14**, 706–720.

WHITE, F. 1999 *Fluid Mechanics*, 4th edn. McGraw-Hill.